

Reconfigurable multi-bit phase change material silicon photonics directional couplers

Ting Yu Teo,^{1,2} Li Lu,¹ and Robert Edward Simpson^{1,3}

¹Singapore University of Technology and Design, 8 Somapah Road, 487372 Singapore, Singapore

²tingyu_teo@mymail.sutd.edu.sg

³robert_simpson@sutd.edu.sg

Abstract

The unique optical properties of phase change materials (PCMs) can be exploited to develop efficient reconfigurable photonic devices. Here, we design, model, and compare the performance of programmable 1X2 optical couplers based on: Ge₂Sb₂Te₅, Ge₂Sb₂Se₄Te₁, Sb₂Se₃, and Sb₂S₃ PCMs. Once programmed, these devices are passive, which can reduce the overall power used in an ONN. In the telecommunication wavelength region (1520 to 1580 nm), the Sb₂S₃ directional coupler displays a minimum insertion loss of -0.04 dB and -1.1 dB, and the lowest crosstalk of -42 dB and -17 dB for the amorphous and crystalline states respectively. We also design a non-volatile 2-bit low-loss tuneable Sb₂S₃ directional coupler that can be used to set the weights of optical neural networks (ONN). Partial crystallization of Sb₂S₃ strips with dimensions compatible to those in the directional coupler indicate that at least four different crystalline lengths can be reliably programmed. We used this effect to design a 2-bit tuneable Sb₂S₃ directional coupler with a weight dynamic range close to 17 dB. The bit-depth of the coupler appears to be limited by the crystallization stochasticity.

1. Introduction

Reconfigurability is an important feature for Photonic Integrated Circuits (PICs) - optical neural networks (ONNs). The ability to tune the light intensity and phase enables the network to encode information in optical signals and perform inferencing and learning tasks [1-3]. Optical neural networks require programmable sub-components, such as Mach-Zehnder Interferometers (MZIs). MZIs use optical directional couplers to split incoming light into two coherent waves, and by controlling their phase and intensity, the ONN weights can be programmed into the network [2]. The weighting component is essential for Multiply-Accumulate (MAC) operations in the network [4]. Common tuneable directional couplers make use of thermo-optic or electro-optic effects to tune the refractive index [5-7]. However, they require a continuous power supply to maintain the optical states. For example, ONN weights that make use of the thermo-optic or electro-optic effect require an additional 10 mW for each synapse [8]. This is non-ideal as the network becomes inefficient when processing large amounts of data, and ultimately the power requirement limits the scale of the network.

Incorporating Chalcogenide phase change materials (PCMs) into directional couplers to introduce tuneability is a better solution because the PCM does not require a power to hold its optical state. Moreover, many PCMs can reversibly switch between their amorphous and crystalline states on a sub-nanosecond time scale [9, 10]. These properties provide a means to design sophisticated tuneable directional couplers [11-13].

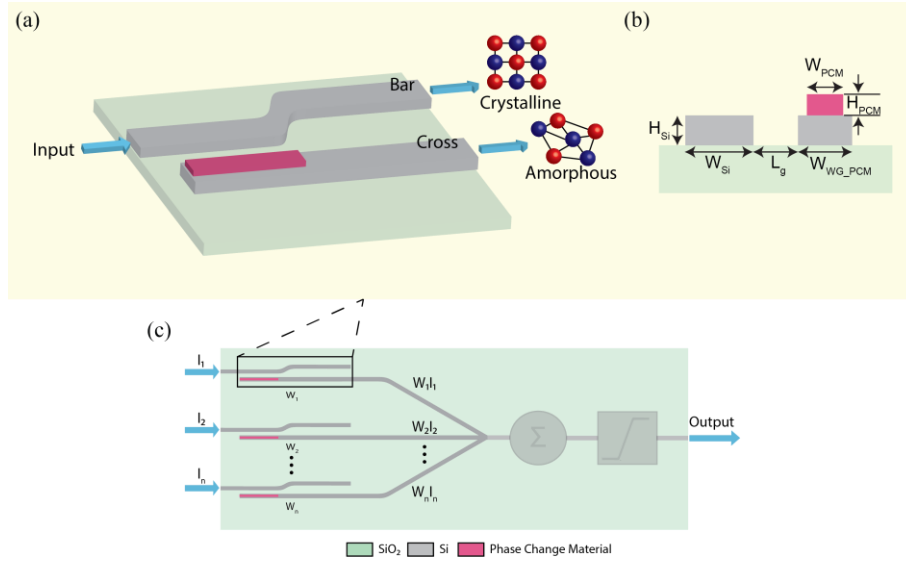


Fig. 1. PIC ONN weights. (a) PCM directional coupler switching operation. In the amorphous state the output signal is at the cross port due to evanescent coupling. In the crystalline state, the signal stays in the same waveguide due to phase mismatch between the two waveguides. (b) Cross section of the PCM directional coupler. The labelled dimensions are critical when designing the couplers. (c) Neural network weight design using PCM-tuned directional coupler. The two-port system design maximizes device performance. This will be discussed at greater length in section 2.

A 1X2 PCM directional coupler was designed that consists of two output waveguide ports, with one waveguide containing a layer of PCM deposited as shown in Fig. 1a. Fig. 1b shows the parameters to be determined when designing PCM directional couplers. The PCM directional coupler is designed to evanescently couple light into the PCM-integrated waveguide port (cross) in the amorphous state. Crystallizing the PCM decreases the amplitude of the evanescent field, and the light remains in the input Si waveguide (bar) port. This design exploits the large refractive index change between the two PCM structural states to control the phase matching condition between the waveguides.

Previous works [11-13] have demonstrated the reconfigurable functionality in PCM directional couplers. However, the actual implementation of PCM directional couplers in ONNs require further material optimization and characterization of the PCM layer. $\text{Ge}_2\text{Sb}_2\text{Te}_5$ and $\text{Ge}_2\text{Sb}_2\text{Se}_4\text{Te}_1$ have been used in PCM directional couplers because they display a large change in refractive index, Δn , upon phase transition. However, they exhibit non-negligible losses at 1550 nm in the crystalline state [14]. Again, for ONNs, this is non-ideal because the cumulative optical energy will decay exponentially with each layer of neurons. To avoid these high optical losses, the low-loss PCMs, Sb_2S_3 and Sb_2Se_3 , were proposed as alternatives to the more traditional Te-based data storage PCMs. Previous works [15-17] showed that both materials exhibit distinguishable optical properties upon a structural phase transition and have a lower extinction ratio than $\text{Ge}_2\text{Sb}_2\text{Te}_5$ and $\text{Ge}_2\text{Sb}_2\text{Se}_4\text{Te}_1$.

The inference accuracy of a neural network depends on the bit-depth of the weights [18, 19]. For practical networks, therefore, the PCM directional couplers must be enhanced to implement multi-level switching. PCM directional couplers that operate with the two distinct structural states can only perform binary switching [11, 12]. To achieve multi-level switching, we have previously proposed amorphizing selected regions of the PCM-waveguide by writing with a focused laser [20]. However, this requires a bulky and complicated setup to amorphize sections of the strip. A simpler and more flexible weight programming method would involve partially crystallizing the entire PCM strip [21-24]. Partial crystallization can be carried out by laser-induced heating [22, 23] or electrical Joule heating [25].

To address the high optical attenuation of the telluride PCM-tuned couplers, herein we design low-loss Sb_2S_3 -programmed directional couplers for ONNs. In addition, we show that when narrow strips of Sb_2S_3 are annealed above the crystallization temperature, crystal growth tends to proceed progressively along the strip, and the length crystallized can be controlled easily with temperature. This effect can be used to implement partial crystallization, which in turn gives multiple optical transmission states. Essentially, we have designed low-loss multi-state directional couplers that can be adopted by those designing ONN systems. Fig. 1c shows the proposed design of ONN weights implemented with tuneable PCM directional couplers.

2. Low-loss PCM Directional Coupler Design and Modelling

To design the PCM-tuned coupler, we consider the four different potentially useful PCMs: $\text{Ge}_2\text{Sb}_2\text{Te}_5$, $\text{Ge}_2\text{Sb}_2\text{Se}_4\text{Te}_1$, Sb_2Se_3 , and Sb_2S_3 . Sb_2S_3 and Sb_2Se_3 both have a very low extinction coefficient (k) in the near infrared, as shown in Fig. 2. Both materials were proposed as lower loss alternatives to $\text{Ge}_2\text{Sb}_2\text{Te}_5$ and $\text{Ge}_2\text{Sb}_2\text{Se}_4\text{Te}_1$, which were previously used to program integrated photonics devices. Fig. 2 shows the optical constants of the four materials. The values of GST, GSST and Sb_2Se_3 were extracted from references [12, 15, 26] whilst the optical constants of Sb_2S_3 were measured by ellipsometry in our lab. Generally, there is a decrease in k when one moves up the Chalcogen group of the periodic table (from Te to Se to S) due to the optical band gap opening [27] and we see this clearly from the optical constant values at 1550 nm shown in Fig. 2. A wavelength of 1550 nm corresponds to a photon energy of 0.8 eV and the bandgap of amorphous $\text{Ge}_2\text{Sb}_2\text{Te}_5$ is 0.7 eV in the amorphous state and 0.5 eV in the face-centered cubic state [28]. Hence, 1550 nm light is absorbed by interband transitions in $\text{Ge}_2\text{Sb}_2\text{Te}_5$. In contrast, the bandgap of Sb_2S_3 is 2.05 eV in the amorphous state and 1.9 eV in the crystalline state. Thus, it has the smallest k due to its largest optical bandgap [16]. Despite its large bandgap, Sb_2S_3 can be switched by either laser heating with above-bandgap light, heating with below bandgap light and using a resonant structure, or using electrical Joule heat-induced phase transitions [16]. Unlike crystalline $\text{Ge}_2\text{Sb}_2\text{Te}_5$, Sb_2S_3 was recently shown to exhibit birefringence [17]. This difference stems from the Sb_2S_3 crystal domains being larger than the wavelength of light, whereas the domains in $\text{Ge}_2\text{Sb}_2\text{Te}_5$ are below the diffraction limit, and therefore the polycrystalline film exhibits an isotropic refractive index. Amorphous marks that were smaller than the diffraction limit could also be written into Sb_2S_3 thin films using femtosecond pulses at 780 nm [17]. This result implies that Sb_2S_3 might be suitable for designing multi-bit programmable couplers. Delany *et al.* also showed that Sb_2S_3 and the related material, Sb_2Se_3 , can be used to tune standard silicon-on-insulator (SOI) waveguide switches with a higher figure of merit (FOM) values than $\text{Ge}_2\text{Sb}_2\text{Te}_5$ [15]. Further studies are required to incorporate the materials into different types of reconfigurable photonic components. Moreover, the crystallization kinetics of this new class of phase change material should be studied to devise efficient switching methods and introduce multiple switching states, which will enhance the reconfigurable functionality of the devices. Hence, this work focuses on designing directional couplers with the low-loss phase change materials and studying the crystallization of Sb_2S_3 when it is patterned with dimensions similar to that of the waveguide.

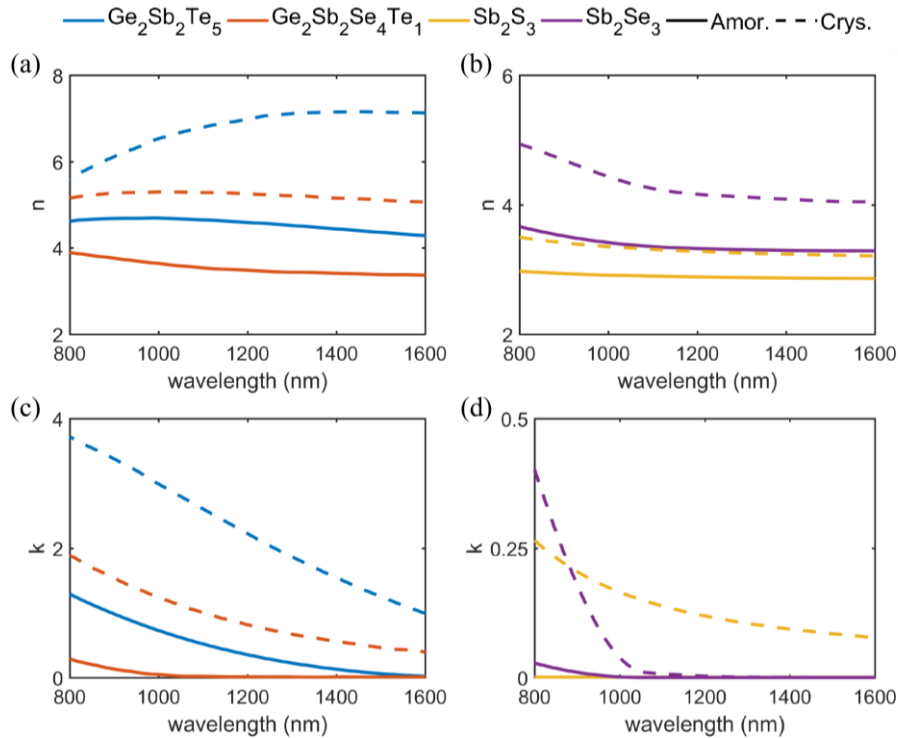


Fig. 2. Optical properties of the four PCMs. Refractive index of (a) GST and GSST, (b) Sb_2S_3 and Sb_2Se_3 , Extinction coefficient of (c) GST and GSST, (d) Sb_2S_3 and Sb_2Se_3 in their respective amorphous and crystalline states.

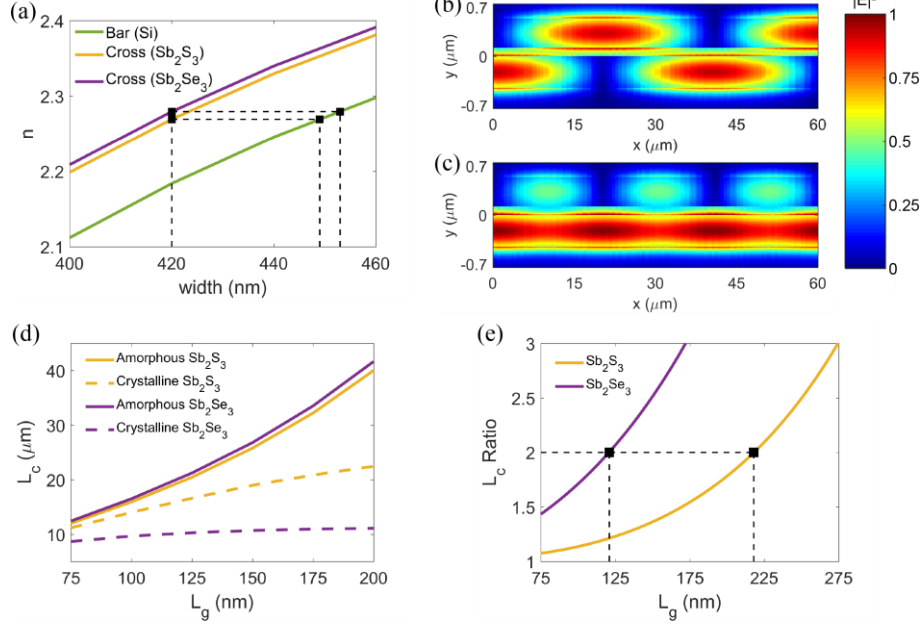


Fig. 3. PCM waveguide design process. (a) Waveguide width optimisation for phase matching between bar and corresponding cross waveguides. Optical field intensity propagation for (b) amorphous and (c) crystalline Sb₂Se₃ when $L_{c,amor} \approx 2n \cdot L_{c,crys}$, where $n \in \mathbb{Z}^+$. The optical signal propagates through different waveguide ports depending on the PCM state, consistent to current PCM directional coupler switching behavior. (d) Coupling length of amorphous and crystalline Sb₂S₃ and Sb₂Se₃, and (e) Coupling length ratio of Sb₂S₃ and Sb₂Se₃.

We modelled Ge₂Sb₂Te₅, Ge₂Sb₂Se₄Te₁, Sb₂Se₃, and Sb₂S₃ Silicon-waveguide directional couplers. The devices were optimized in the transverse electric (TE) mode. Silicon-based couplers were chosen due to their wide applicability in integrated photonics and integrability with electronic integrated circuits. When designing PCM directional couplers, the dimensions shown in Fig. 1b are to be determined. They are the (a) dimensions of the phase change material, cross, and bar waveguide, (b) coupling gap between the two waveguides, L_g , and (c) the coupling length, L_c . L_c is equivalent to the length of the phase change material. The waveguide dimensions were chosen to ensure single-mode operation. Hence, the cross-waveguide widths were fixed at 420 nm and the height of all waveguides were fixed at 220 nm. The widths of the bar waveguides were selected to satisfy the phase matching condition in the amorphous state [11]. Fig. 3a shows the waveguide dimensions required to attain phase matching conditions for the two materials. The effective refractive indices of the cross and bar waveguides, n_{eff} , were calculated using the MODE solution waveguide solver in Lumerical [29]. The electric field distribution profiles of the PCM waveguides with the optimized dimension and the corresponding n_{eff} values can be found in the supplementary document Fig. S1 and Table S1 respectively. The choice of L_g was critical when designing Sb₂S₃ directional couplers. This is because the Δn at 1550 nm between the crystalline and amorphous states is smaller than GST and GSST. For GST and GSST, the larger Δn upon phase transition caused a large phase mismatch between the two waveguides in the crystalline state. Hence, the input signal did not couple into the cross-waveguide in the crystalline state. L_g was thus chosen to optimize the trade-off between insertion loss in the crystalline state and a longer device coupling length [11]. However, for PCMs with a smaller Δn , the phase mismatch in the crystalline state was not as large and the coupling gap needs to be optimized to allow the coupling length in the amorphous state to be a common multiple of the coupling length in the crystalline state. This allowed the optical signal to couple back into the bar-waveguide in the fully crystallized state. Lumerical's Eigenmode Expansion solver (EME) was used to demonstrate that this requirement is necessary [29]. For clarity and analysis, the field propagation patterns in the amorphous and crystalline state of an Sb₂Se₃ directional coupler are given in Figs. 3b and 3c, respectively. Since the effective coupling length of the directional coupler must allow the signal to exit at the different ports upon phase transition, the coupling length of each structural state must be an even multiple from each other: $L_{c,amor} \approx 2n \cdot L_{c,crys}$ where $n \in \mathbb{Z}^+$. To minimize the footprint and coupling losses, we choose the lowest common even multiple, where $n = 1$.

The coupling length, L_c , was calculated using the coupled wave theory equation [11, 30]: $L_c = \frac{\lambda}{2(n_1 - n_2)}$, where λ is the wavelength, and n_1 and n_2 are the effective indices of the odd and even supermodes in a two-waveguide system. Again, the values of n_1 and n_2 were calculated using the MODE solution solver within Lumerical. The

electric field distribution patterns and the calculated values of the two-waveguide system can be found in Fig. S1 and Tables S2a and S2b respectively.

Upon stipulating the design requirements and calculations, the coupling gap, L_g , and length, L_c , of the Sb_2S_3 and Sb_2Se_3 directional couplers were then determined according to Figs. 3d and 3e. Fig. 3d shows the corresponding L_c of the materials for the different structural state as L_g increases. For clarity, we represent the L_c of the two structural states as a ratio i.e. L_c ratio = $\frac{L_{c,amor}}{L_{c,crys}}$ in Fig. 3e. L_g was chosen to give a L_c ratio of two. The final dimensions of the PCM directional coupler are represented in a Table 1. For comparison purposes, GST and GSST directional couplers were also modelled.

Table 1. Device dimensions and switching time for the various PCM-tuned directional couplers.

Material	PCM Width (nm)	PCM Height (nm)	Si Waveguide Width (nm)	Coupling Gap (nm)	Coupling Length (μm)	Switching time (ns), thickness (nm)
 $\text{Ge}_2\text{Sb}_2\text{Te}_5$ ^[22]	320	20	456	107	18.407	50, 60
 $\text{Ge}_2\text{Sb}_2\text{Se}_4\text{Te}_1$ ^[10]	320	30	448	150	25.861	$100*10^6$, 40
 Sb_2S_3	400	40	449	218	46.706	78, 20
 Sb_2Se_3 ^[13]	400	30	453	121	20.415	$100*10^6$, 50

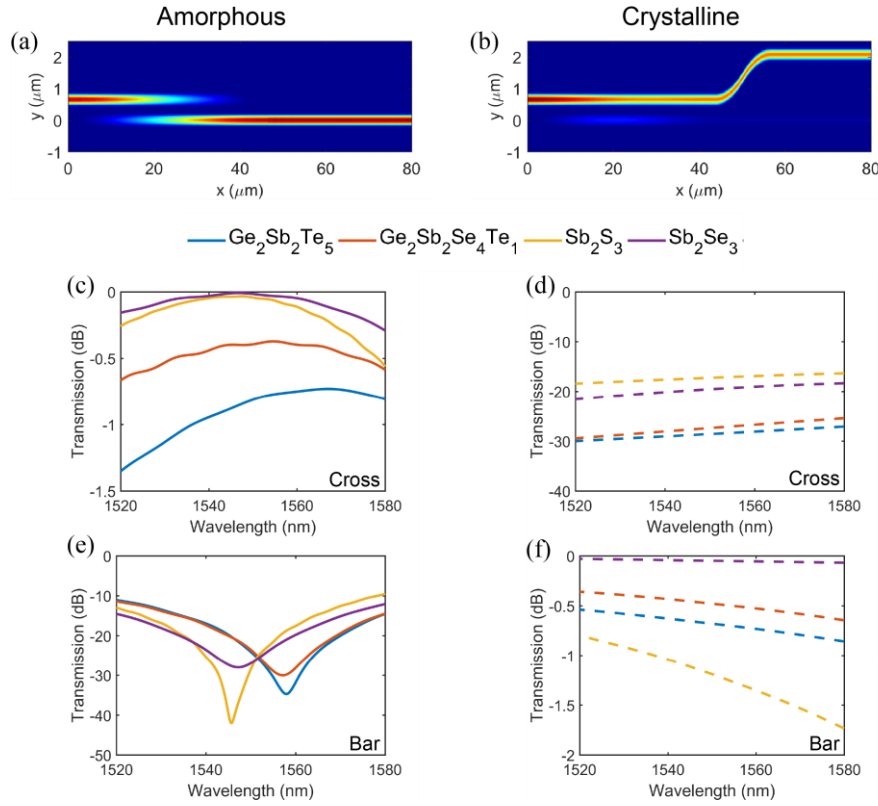


Fig. 4. PCM Directional coupler performance. Normalised power distribution (in arbitrary units) of (a) amorphous Sb_2S_3 and (b) crystalline Sb_2S_3 . The insertion loss of the coupler in the (c) amorphous and (f) crystalline state and crosstalk in the (d) amorphous and (e) crystalline state.

The insertion loss and cross talk for all four PCM couplers were analyzed in the telecommunication conventional band (1520 nm to 1580 nm) using a finite difference time domain (FDTD) approach to solve Maxwell's equations. Insertion loss represents the proportion of light that is transmitted through the coupler while the crosstalk represents the proportion of light in the inactive output port. The results are shown in Fig. 4. Figs. 4a and 4b show the power distribution of the coupler device when Sb_2S_3 is in the amorphous and crystalline state respectively. The corresponding insertion loss and crosstalk of the device, from a wavelength of 1520 nm to 1580 nm, are presented in figs. 4c to 4f. All the PCM directional couplers studied had an insertion loss below -1.5 dB and crosstalk between -10 dB to -42 dB in the amorphous state. In the crystalline state, the insertion loss was found to be below -2 dB and the crosstalk was between -17 dB and -30 dB. The switching characteristic of the Sb_2S_3 and Sb_2Se_3 directional couplers is consistent with previous works [11, 12], which adds a degree of confidence to the analysis of the coupler designs.

Low-loss PCM-tuned Sb_2S_3 and Sb_2Se_3 couplers have the highest transmission when the PCM is completely amorphous. The Sb_2S_3 device in the amorphous state exhibited the lowest crosstalk of all devices, at -42 dB. Moreover, the insertion loss for Sb_2S_3 and Sb_2Se_3 devices was below -0.6 dB, which is substantially lower than that of the GST and GSST devices. However, upon crystallization, the insertion loss and crosstalk of Sb_2S_3 and Sb_2Se_3 -tuned devices became greater. The higher insertion loss for the crystalline state was due to coupling losses when the signal coupled back to the bar waveguide. The remaining light in the cross-waveguide resulted in a crosstalk value of -17 dB and -20 dB for Sb_2S_3 and Sb_2Se_3 respectively, which is relatively low. The insertion loss of Sb_2S_3 was higher in the crystalline state due to the wider coupling gap between the two waveguides. Sb_2S_3 directional couplers required a larger gap to obtain the $L_{c,amor} \approx 2 \cdot L_{c,crys}$ condition, as illustrated in Fig. 3e. This was because the change in coupling length from the amorphous to crystalline state was smaller for Sb_2S_3 , as shown in Fig. 3d. The smaller change is attributed to the smaller phase mismatch between the cross and bar waveguides in the crystalline Sb_2S_3 state. Hence, the $L_{c,amor} \approx 2 \cdot L_{c,crys}$ condition was only met when the coupling gap was wider.

The results in Fig. 4 show that Sb_2S_3 is the most suitable material for programmable low-loss optical couplers. This is because in the amorphous state, the coupler insertion loss is lower than the Tellurium-based PCMs, and the crosstalk is the lowest of all the PCMs studied. Note, the optical constants used in these models may have caused an artificially higher insertion loss in Sb_2S_3 than Sb_2Se_3 . In Delaney *et al.* work, both materials have a zero extinction coefficient in the amorphous and crystalline state at the telecommunication wavelength [15]. However, at the same wavelength, our ellipsometry measurements show non-zero extinction ratio for both the amorphous and crystalline phases of Sb_2S_3 . We believe, therefore, that the extinction ratio of Sb_2Se_3 will be larger than our measured Sb_2S_3 data due to the bandgap of Sb_2Se_3 being smaller than Sb_2S_3 [27]. The higher absorption of Sb_2Se_3 is also evident in Delaney *et al.* measurements where the extinction ratio of Sb_2Se_3 is higher than Sb_2S_3 before 1550 nm [15]. Hence, we expect the insertion loss of the Sb_2S_3 coupler to be lower than the current results if we used Delaney *et al.* ellipsometry data with zero extinction ratio values. Aside from these device properties, the switching time of Sb_2S_3 is also very fast at just 70 ns [16]. A spider diagram comparing the performance of the different PCM couplers is shown in Fig. 5.

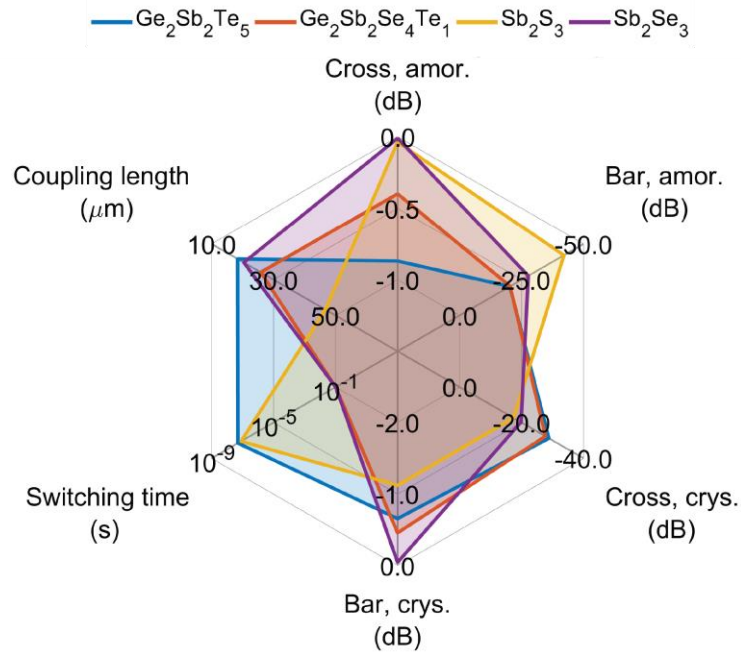


Fig. 5. Radar chart that compares the performance of the four PCM directional couplers. The axes are arranged such that the desirable properties are on the edge of the chart.

For ONN applications, insertion loss must be minimized as it limits the depth of the network and concomitantly limits the complexity of the data that can be analyzed [4]. Importantly, Sb_2S_3 has the lowest amorphous state insertion loss of all the PCMs studied, which makes it suitable for many neural layers. Although the crystalline state insertion loss for Sb_2S_3 is higher than Sb_2Se_3 , the two-waveguide system design, which is shown in Fig. 1c, can be used to mitigate these losses. When Sb_2S_3 is in the amorphous state, the switch is turned on and the cross output port receives almost the full input signal. Indeed, we see that the transmission is better than 99 % or 0.03 dB at 1550 nm. After completely crystallizing the Sb_2S_3 layer, the cross-port is switched off and the signal is coupled back into the bar-waveguide. The remaining signal in the cross-waveguide is suppressed by -17 dB, which equates to a crosstalk of lower than 0.02%. The high insertion loss is avoided as the signal goes through the inactive bar port. Hence, the high insertion loss problem faced by Sb_2S_3 directional couplers in the crystalline state is not intrinsic to the material and can be mitigated with engineering solutions. $\text{Ge}_2\text{Sb}_2\text{Te}_5$ and $\text{Ge}_2\text{Sb}_2\text{Se}_4\text{Te}_1$ directional couplers can also be designed to avoid the higher insertion losses in the amorphous state by setting the bar waveguide as the output port. However, the performance of these designs will be worse than Sb_2S_3 -based couplers because the insertion loss will still be higher than that of the amorphous Sb_2S_3 device. As a rule, therefore, it is preferable to select PCMs with the lowest insertion loss in the amorphous state.

Intermediate switching states are an essential feature of ONN weights. Partial crystallization of the PCM layer can be used to introduce multi-level optical states into a photonics device. When crystallized to varying extents, the optical constant of the material changes. There are essentially two ways to exploit crystallization to create a multilevel optical device and these depend on how the material crystallizes. Crystallization of some materials is dominated by nucleation. For example, $\text{Ge}_2\text{Sb}_2\text{Te}_5$ exhibits a high density of crystal nuclei once it is heated above its crystallization temperature. This means that the crystallites tend to be small, and the growth time is short. Other materials, such as AIST and Sb_2S_3 , do not easily nucleate and the crystallites grow large from very few nucleation centers. Sb_2S_3 does not easily nucleate hence large crystallites are seen [17]. If the crystallites are substantially smaller than the wavelength of light, then the effective refractive index of the partially crystallized material can be derived with the Clausius-Mossotti relation [31, 32]. On the other hand, for Sb_2S_3 , where the crystallites tend to be larger than the wavelength of light, it is more appropriate to compute the multiple transmission levels by solving Maxwell's equations for reflection and transmission of light propagating through the two material domains.

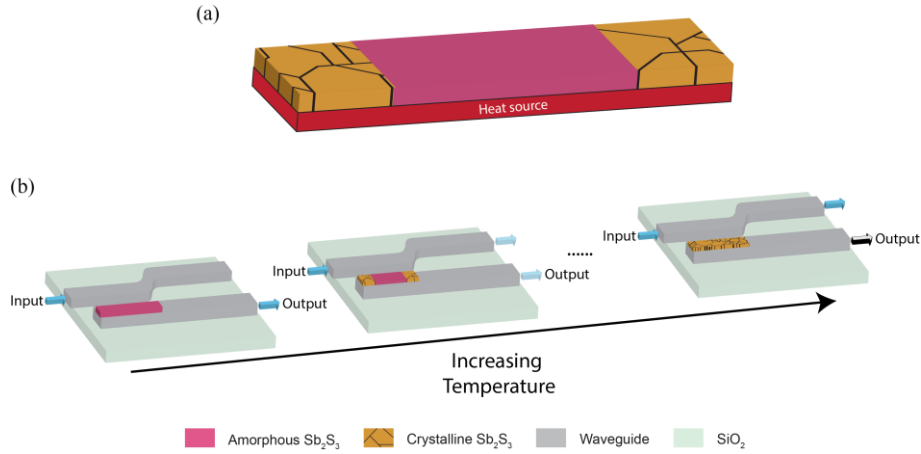


Fig. 6. Schematic of Growth Crystallization Tuning (GCT) mechanism (a) Imbedded heat source in the system to crystallize PCM (b) Tunable coupling ratio due to PCM crystallizing to different extent. The coupling ratio is controlled by the temperature of heat source as represented by a decreasing output intensity signal.

We can also envisage multiple ways to crystallize the PCM couplers. The first way might be by using a laser to heat the PCM and create crystalline pixels along the waveguide length. However, this might be impractical for a small-scale device. A more practical design might include an imbedded heater below the PCM [25]. Since Sb_2S_3 is dominated by crystal growth, this heater could be used to controllably crystallize strips of Sb_2S_3 to different extents, which in turn controls the coupling ratio, see schematic shown in Fig. 6. We name this method Growth Crystallization Tuning (GCT).

To exploit GCT in Sb_2S_3 -tuned Si waveguide directional couplers, we first must understand how the Sb_2S_3 strips crystallize. Therefore, we patterned Sb_2S_3 cuboids of dimension $46.7 \mu\text{m}$ by $0.4 \mu\text{m}$ by 40 nm (Length by Width by Height) on a Silica on Si substrate. These dimensions were selected to match those of the optimized coupler design, see Table 1. The strips were fabricated in the following sequence: (a) Electron Beam Lithography patterning, (b) Material deposition with Radio Frequency (RF) Magnetron Sputtering and (c) Material lift-off. We first deposit an 89 nm PMMA 950K A2 photoresist on the substrate by spin coating at 2000 RPM for 60 seconds . Electron beam lithography was then performed using the Raith eLINE Plus lithography system to pattern the Sb_2S_3 strips. The operating beam voltage was at 30 kV with an aperture size of $30 \mu\text{m}$. The photoresist was then developed using the MIBK: IPA developer of ratio 1:3. Subsequently, we deposited Sb_2S_3 on the resist pattern using a 50.8 mm diameter 99.9% pure Sb_2S_3 target using the AJA Orion 5 sputtering system with a base pressure of $2.3 \times 10^{-7} \text{ Torr}$. The sputtering process took place in an Argon environment at a pressure of $3.7 \times 10^{-3} \text{ Torr}$. The RF power was set to 20 W , which resulted in a deposition rate of 0.15 \AA/s . After Sb_2S_3 deposition, the photoresist was removed by soaking the sample in a 1-Methyl-2-pyrrolidinone (NMP) solution placed in a $60 \text{ }^\circ\text{C}$ water bath for one hour. The sample was then rinsed with Acetone followed by Isopropyl Alcohol, before drying it with N_2 gas. An SEM image of a typical Sb_2S_3 strip is given in Fig. S2.

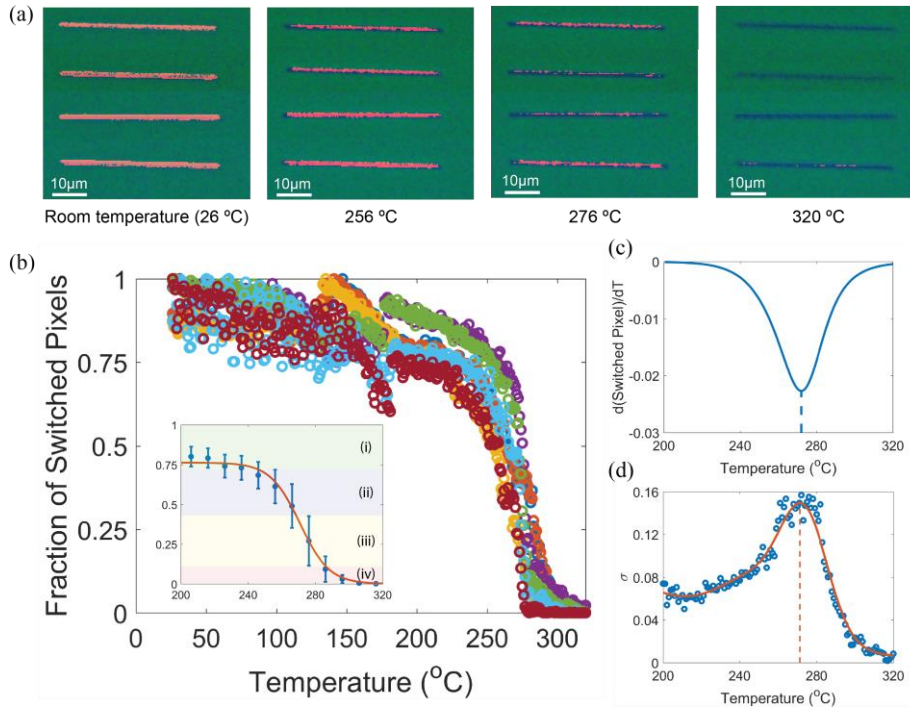


Fig. 7. Crystallization profile of Sb₂S₃ strips. (a) False color optical images of the Sb₂S₃ strip taken during the heating process. The color change represents phase transition. Pink and blue pixels represent amorphous and crystalline regions respectively (b) Fraction of switched pixels with respect to temperature of the seven Sb₂S₃ strips. Inset in (b) shows the average and standard deviation of the fraction of crystallized pixel across the seven strips. The regions (i) to (iv) represent the four switching states that can be achieved. (c) Averaged differential of the seven switching curves in (b). The trough represents the average crystallization temperature. (d) Standard deviation of switched pixels with respect to temperature. The peak occurs at the crystallization temperature due to the stochastic nature of Sb₂S₃ crystallization.

The Sb₂S₃ strip crystallization behavior was studied by tracking the change in optical reflectivity normal to the strip's surface. The samples were heated to 320 °C using a heating rate of 5 °C/min in a Linkam microscope furnace (Linkam T95-HT) with an Ar gas flow rate of 4 SCCM. Microscope images of the strips under $\times 10$ magnification were collected for every 1 °C rise in temperature, i.e. at a rate of 5 images per minute. The strip increased in reflectivity during crystallization, which allowed the crystal growth to be monitored [33]. False color optical microscope images of the strips are shown in Fig. 7a where the amorphous and crystalline regions are shown as pink and blue, respectively. The strips tend to crystallize inwards from the edges. These results show that Sb₂S₃ strip crystallization is growth driven, as is also seen in continuous films [34]. Fig. 7b shows the fraction of crystallized pixels for seven different Sb₂S₃ strips as a function of temperature. For clarity and further analysis, the average and standard deviation of the fraction of switched pixels for every 10 °C rise in temperature is given in the inset of Fig. 7b. The average crystallization temperature is 270 ± 5 °C as shown in Fig. 7c.

The stochastic nature of Sb₂S₃ crystallization affects the levels of ONN weights. From Fig. 7d. we see that the standard deviation of switched pixels is largest at 270 °C, when the rate of crystallization is maximum. This is due to the strips crystallizing at slightly different temperatures. This variation can be attributed to the growth-driven crystallization kinetics. As nucleation is a stochastic process, the number of nucleation centers in the strip is random. This variability in crystallization was previously attributed to material defects [15], but is more likely due to the stochastic nature of Sb₂S₃ crystallization. Regardless of the origin, this variability will limit the number of switching levels because at a certain temperature the crystallized length of the Sb₂S₃ strip varies.

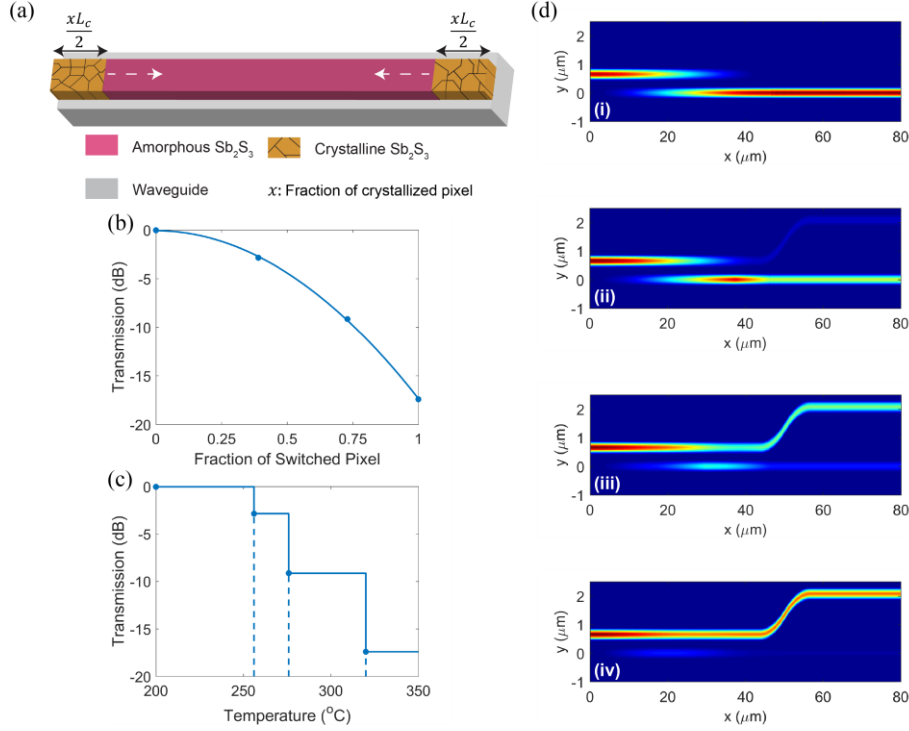


Fig. 8. 2-bit Sb_2S_3 directional coupler. (a) Partial crystallization model of the cross waveguide. The strip is sectioned into the amorphous and crystalline regions based on the experimentally measured fraction of crystallized pixels. Since the material tends to crystallize inwards from the end, the crystalline regions increase along the direction of the white arrows with increasing temperature. (b) Transmission through the cross output port for the four crystalline lengths. (c) Operating temperature regions of the four switching states (d) Power distribution of the Sb_2S_3 directional coupler base on the crystallization percentage. Labels (i) to (iv) correspond to the colored regions in inset of Fig. 7b.

Temperature can be used to control the output power of the coupler to four distinguishable transmission levels with a dynamic range of 16.96 dB. Using the standard deviation of switched pixels at different temperatures, the extent of crystallization can be statistically discerned into four levels. The states are represented as regions (i) to (iv) in the inset of Fig. 7b. To model the effect of partial crystallization on the waveguide transmission, the Sb_2S_3 strip in the coupler model was sectioned to the corresponding amorphous and crystalline regions. As the strip crystallizes inwards from the edges, we varied the length of the crystalline regions along the direction of the white arrows shown in Fig. 8a. The crystallized lengths of the two intermediate states are proportional to the fraction of switched pixels. 3D FDTD simulations were conducted to determine the directional coupler Cross and Bar transmissivity for each of the four discernable levels of crystallinity observed in the crystallization experiment in Fig 7b. Fig. 8b shows a two-bit Sb_2S_3 directional coupler performance at 1550 nm. The transmission values range from -0.04 dB and -17 dB, i.e. a dynamic range of 16.96 dB. Fig. 8c shows the operating temperature range for the different states and Fig. 8d illustrates how the power is distributed along the waveguide for each state. We see that by using the GCT method, temperature can be used to tune the cross output port transmissivity to four distinct levels. The four switching states are sufficient to implement 2-bit weighting schemes in a quantized neural network. Quantized network schemes have been proposed to down-scale deep neural networks in space-limited platforms, such as mobile devices [35]. Moreover, the large dynamic range of almost 17 dB suggests that higher bit-depths can be accommodated if the crystallization stochasticity is minimized or avoided.

Decreasing crystallization stochasticity will increase the bit-depth of the weights and thus improve inference accuracy of ONNs. In addition to GCT, the two methods in Fig. 9 can be adopted to further increase the Sb_2S_3 coupler bit-depth. In the first method shown in Fig. 9a, the initial state of the Sb_2S_3 layer is crystalline and the entire length is partially amorphized to varying degrees to achieve the different switching states. Previous works have amorphized Sb_2S_3 thin films to varying degrees with a femtosecond laser to produce nano prints [17]. The second method, which is shown in Fig. 9b, involves fully amorphizing regions of a crystalline Sb_2S_3 strip to implement the different switching states. The transmission level is then set by the length of the amorphous strip. Both processes use the fact that amorphisation is more deterministic than crystallization and therefore the transmissivity can be controlled more accurately. We recommend selecting the appropriate method specific for the ONN purpose. We previously showed Sb_2S_3 can be amorphized with 5 ns laser pulses [16], hence these

methods may be suitable for online training networks that require weights to be programmed accurately at high speeds.

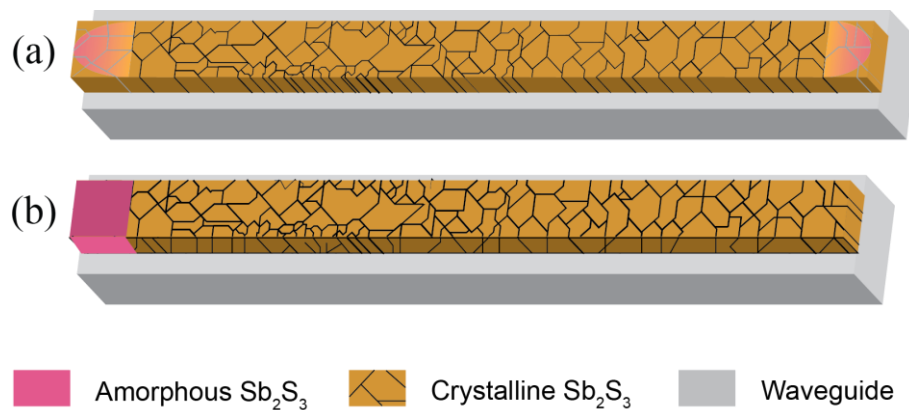


Fig. 9. Weight programming methods to minimize or avoid crystallization stochasticity. (a) Amorphizing the entire crystalline Sb_2S_3 strips to varying degrees to implement different switching states. This reduces stochasticity as nucleation of the material is avoided. (b) Amorphizing regions on the crystalline strip to implement the various switching states. Weights are tuned by amorphizing different length of the strip, which is more deterministic than crystal nucleation and growth.

3. Conclusion

To conclude, Sb_2S_3 -tuned directional couplers are suitable for setting the weights in low-loss ONN applications. We demonstrated that these devices exhibit a low insertion loss of less than -0.04 dB and low cross talk better than -40 dB in the amorphous state. With the two-port waveguide design, the high insertion loss in the crystalline state can be avoided. The Sb_2S_3 -tuned directional couplers have a dynamic range close to 17 dB, and by considering the stochasticity of crystallization, we reason that four transmission levels are distinguishable. Ultimately, the choice of PCM depends on the design requirements of each network. Low-loss PCMs are better suited for deeply connected networks. However, the footprint will be larger than devices based on $\text{Ge}_2\text{Sb}_2\text{Te}_5$ due to the smaller refractive index change between the amorphous and crystalline states at 1550 nm. For online training networks, $\text{Ge}_2\text{Sb}_2\text{Te}_5$ and Sb_2S_3 are more suitable than $\text{Ge}_2\text{Sb}_2\text{Se}_4\text{Te}_1$ and Sb_2Se_3 because their switching speed can be very high. We presented a method where the temperature of the Sb_2S_3 strip is used to control the extent of crystallization, and this in turn can be used to tune the coupling ratio. In this design, randomness in the crystallization process limits the number of levels that can be reliably set. Hence, to increase the number of distinct coupling ratios, programming Sb_2S_3 needs to be modified to make the crystal to amorphous ratio more deterministic. Overall, this work shows that Sb_2S_3 is the most appropriate PCM for designing programmable couplers for low loss Si photonics neural networks.

Funding. Agency for Science, Technology and Research (A*STAR), Grant number: #A18A7b0058

Acknowledgement. This work was supported by an A*Star Advanced Manufacturing and Engineering programmatic grant (#A18A7b0058). The work was carried out under the auspices of the SUTD-MIT International Design Centre. LL is grateful for his Ministry of Education Singapore PhD scholarship.

Disclosures. The authors declare no conflicts of interest.

Data Availability. Data underlying the results presented in this paper are not publicly available at this time but may be obtained from the authors upon reasonable request.

Supplemental document. See Supplement 1 for supporting content.

References

1. Z. Cheng, C. Ríos, W. H. P. Pernice, C. D. Wright, and H. Bhaskaran, "On-chip photonic synapse," *Science Advances* **3**, e1700160 (2017).
2. Y. Shen, N. C. Harris, S. Skirlo, M. Prabhu, T. Baehr-Jones, M. Hochberg, X. Sun, S. Zhao, H. Larochelle, D. Englund, and M. Soljačić, "Deep learning with coherent nanophotonic circuits," *Nature Photonics* **11**, 441-446 (2017).

3. J. George, R. Amin, A. Mehrabian, J. Khurgin, T. El-Ghazawi, P. R. Prucnal, and V. J. Sorger, "Electrooptic Nonlinear Activation Functions for Vector Matrix Multiplications in Optical Neural Networks," in *Advanced Photonics 2018 (BGPP, IPR, NP, NOMA, Sensors, Networks, SPPCom, SOF)*, OSA Technical Digest (online) (Optical Society of America, 2018), SpW4G.3.
4. M. Miscuglio, G. C. Adam, D. Kuzum, and V. J. Sorger, "Roadmap on material-function mapping for photonic-electronic hybrid neural networks," *APL Materials* **7**, 100903 (2019).
5. J.-S. Kim and J. T. Kim, "Silicon electro-optic modulator based on an ITO-integrated tunable directional coupler," *Journal of Physics D: Applied Physics* **49**, 075101 (2016).
6. X. Zi, L. Wang, K. Chen, and K. S. Chiang, "Mode-Selective Switch Based on Thermo-Optic Asymmetric Directional Coupler," *IEEE Photonics Technology Letters* **30**, 618-621 (2018).
7. M. Thomaschewski, V. A. Zenin, C. Wolff, and S. I. Bozhevolnyi, "Plasmonic monolithic lithium niobate directional coupler switches," *Nature Communications* **11**, 748 (2020).
8. Q. Zhang, H. Yu, M. Barbiero, B. Wang, and M. Gu, "Artificial neural networks enabled by nanophotonics," *Light: Science & Applications* **8**, 42 (2019).
9. D. Loke, T. H. Lee, W. J. Wang, L. P. Shi, R. Zhao, Y. C. Yeo, T. C. Chong, and S. R. Elliott, "Breaking the Speed Limits of Phase-Change Memory," *Science* **336**, 1566 (2012).
10. L. Waldecker, T. A. Miller, M. Rude, R. Bertoni, J. Osmond, V. Pruneri, R. E. Simpson, R. Ernstorfer, and S. Wall, "Time-domain separation of optical properties from structural transitions in resonantly bonded materials," *Nat Mater* **14**, 991-995 (2015).
11. P. Xu, J. Zheng, J. K. Doyle, and A. Majumdar, "Low-Loss and Broadband Nonvolatile Phase-Change Directional Coupler Switches," *ACS Photonics* **6**, 553-557 (2019).
12. Q. Zhang, Y. Zhang, J. Li, R. Soref, T. Gu, and J. Hu, "Broadband nonvolatile photonic switching based on optical phase change materials: beyond the classical figure-of-merit," *Opt. Lett.* **43**, 94-97 (2018).
13. Y. Ikuma, T. Saiki, and H. Tsuda, "Proposal of a small self-holding 2*2 optical switch using phase-change material," *IEICE Electronics Express* **5**, 442-445 (2008).
14. M. Wuttig, H. Bhaskaran, and T. Taubner, "Phase-change materials for non-volatile photonic applications," *Nature Photonics* **11**, 465 (2017).
15. M. Delaney, I. Zeimpekis, D. Lawson, D. W. Hewak, and O. L. Muskens, "A New Family of Ultralow Loss Reversible Phase-Change Materials for Photonic Integrated Circuits: Sb₂S₃ and Sb₂Se₃," *Advanced Functional Materials* **30**, 2002447 (2020).
16. W. Dong, H. Liu, J. K. Behera, L. Lu, R. J. H. Ng, K. V. Sreekanth, X. Zhou, J. K. W. Yang, and R. E. Simpson, "Wide Bandgap Phase Change Material Tuned Visible Photonics," *Advanced Functional Materials* **29**, 1806181 (2019).
17. H. Liu, W. Dong, H. Wang, L. Lu, Q. Ruan, Y. S. Tan, R. E. Simpson, and J. K. W. Yang, "Rewritable color nanoprints in antimony trisulfide films," *Science Advances* **6**, eabb7171 (2020).
18. S. Yu, "Neuro-inspired computing with emerging nonvolatile memories," *Proceedings of the IEEE* **106**, 260-285 (2018).
19. D. Kuzum, S. Yu, and H. S. Philip Wong, "Synaptic electronics: materials, devices and applications," *Nanotechnology* **24**, 382001 (2013).
20. T. Yu, X. Ma, E. Pastor, J. George, S. Wall, M. Miscuglio, R. Simpson, and V. Sorger, "All-Chalcogenide Programmable All-Optical Deep Neural Networks," (2021).
21. S. R. Ovshinsky, "Optical Cognitive Information Processing – A New Field," *Japanese Journal of Applied Physics* **43**, 4695-4699 (2004).
22. M. Rudé, J. Pello, R. E. Simpson, J. Osmond, G. Roelkens, J. J. G. M. van der Tol, and V. Pruneri, "Optical switching at 1.55 μm in silicon racetrack resonators using phase change materials," *Applied Physics Letters* **103**, 141119 (2013).
23. C. Ríos, M. Stegmaier, P. Hosseini, D. Wang, T. Scherer, C. D. Wright, H. Bhaskaran, and W. H. P. Pernice, "Integrated all-photonic non-volatile multi-level memory," *Nature Photonics* **9**, 725-732 (2015).
24. Y. Meng, J. K. Behera, Y. Ke, L. Chew, Y. Wang, Y. Long, and R. E. Simpson, "Design of a 4-level active photonics phase change switch using VO₂ and Ge₂Sb₂Te₅," *Applied Physics Letters* **113**, 071901 (2018).
25. J. Zheng, Z. Fang, C. Wu, S. Zhu, P. Xu, J. K. Doyle, S. Deshmukh, E. Pop, S. Dunham, M. Li, and A. Majumdar, "Nonvolatile Electrically Reconfigurable Integrated Photonic Switch Enabled by a Silicon PIN Diode Heater," *Advanced Materials* **32**, 2001218 (2020).
26. C. Li Tian, D. Weiling, L. Li, Z. Xilin, B. Jitendra, L. Hailong, V. S. Kandammathe, M. Libang, C. Tun, Y. Joel, and E. S. Robert, "Chalcogenide active photonics," in *Proc.SPIE*, (2017),
27. R. E. Simpson and T. Cao, "Phase Change Material Photonics," (2021), p. 487.
28. B.-S. Lee, J. R. Abelson, S. G. Bishop, D.-H. Kang, B.-k. Cheong, and K.-B. Kim, "Investigation of the optical and electronic properties of Ge₂Sb₂Te₅ phase change material in its amorphous, cubic, and hexagonal phases," *Journal of Applied Physics* **97**, 093509 (2005).
29. L. Inc., <https://www.lumerical.com/products/>.
30. S. Miller, "Coupled wave theory and waveguide applications," *Bell System Technical Journal* **33**, 661-719 (1954).
31. C. H. Chu, M. L. Tseng, J. Chen, P. C. Wu, Y.-H. Chen, H.-C. Wang, T.-Y. Chen, W. T. Hsieh, H. J. Wu, G. Sun, and D. P. Tsai, "Active dielectric metasurface based on phase-change medium," *Laser & Photonics Reviews* **10**, 986-994 (2016).
32. J. Tian, Q. Li, J. Lu, and M. Qiu, "Reconfigurable all-dielectric antenna-based metasurface driven by multipolar resonances," *Opt. Express* **26**, 23918-23925 (2018).
33. N. Yamada, E. Ohno, K. Nishiuchi, N. Akahira, and M. Takao, "Rapid-phase transitions of GeTe-Sb₂Te₃ pseudobinary amorphous thin films for an optical disk memory," *Journal of Applied Physics* **69**, 2849-2856 (1991).
34. W. Zhang, R. Mazzarello, M. Wuttig, and E. Ma, "Designing crystallization in phase-change materials for universal memory and neuro-inspired computing," *Nature Reviews Materials* **4**, 150-168 (2019).
35. J. Choi, S. Venkataramani, V. Srinivasan, K. Gopalakrishnan, Z. Wang, and P. Chuang, "Accurate and Efficient 2-bit Quantized Neural Networks," in *MLSys*, (2019).